Heterojunctions of Halogen-Doped Carbon Nitride Nanosheets and BiOI for Sunlight-Driven Water-Splitting

Kazi M. Alam,[1‡] Pawan Kumar,[1‡] Piyush Kar,[1] Ankur Goswami,[1] Ujwal K. Thakur,[1] Sheng Zeng,[1] Ehsan Vahidzadeh,[1] Kai Cui[2] and Karthik Shankar[1*]

[1]*Department of Electrical & Computer Engineering, University of Alberta, Edmonton, AB T6G 1H9 Canada*

[2]*Nanotechnology Research Centre, National Research Council of Canada, Edmonton, Canada*

**corresponding author's email address: kshankar@ualberta.ca*

‡These authors contributed equally

†Electronic supplementary information (ESI) available. See DOI:

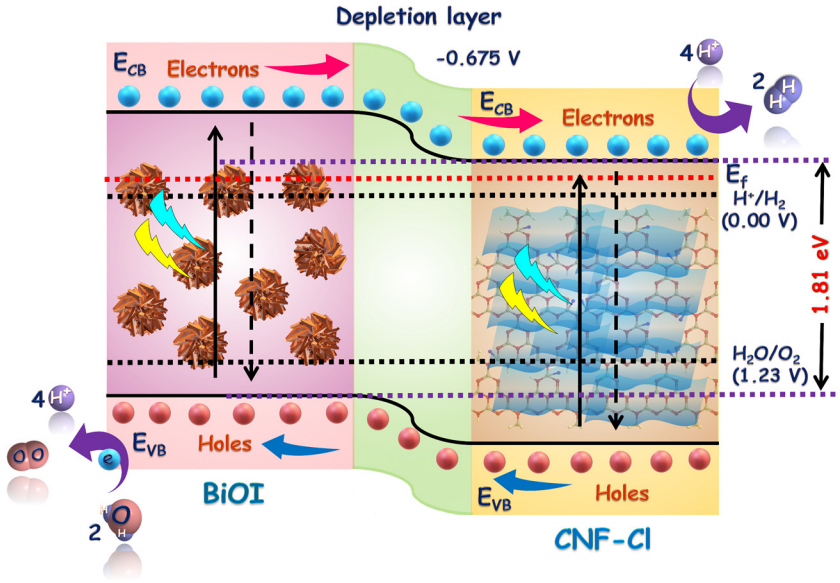

* Tel: 780-492-1354; email: kshankar@ualberta.ca

Abstract

A fluorine-doped, chlorine-intercalated carbon nitride (CNF-Cl) photocatalyst has been synthesized for simultaneous improvements in light harvesting capability along with suppression of charge recombination in bulk g-C_3N_4. The formation of heterojunctions of these CNF-Cl nanosheets with low bandgap, earth abundant bismuth oxyiodide (BiOI) was achieved, and the synthesized heterojunctions were tested as active photoanodes in photoelectrochemical water splitting experiments. BiOI/CNF-Cl heterojunctions exhibited extended light harvesting with a band-edge of 680 nm and generated photocurrent densities approaching 1.3 mA cm^{-2} under AM1.5 G one sun illumination. Scanning Kelvin probe force microscopy (KPFM) under optical bias showed a surface potential of 207 mV for the 50% BiOI/CNF-Cl nanocomposite, while pristine CNF-Cl and BiOI had surface photopotential values of 83 mV and 98 mV respectively, which in turn, provided direct evidence of superior charge separation in the heterojunction blends. Enhanced charge carrier separation and improved light harvesting capability in BiOI/CNF-Cl hybrids were found to be the dominant factors in increased photocurrent, compared to the pristine constituent materials.

Keywords: Carbon nitride nanosheets, earth abundant semiconductors, semiconductor photocatalyst, charge carrier recombination, photophysics of carbon nitrides.

1.0 Introduction

Photocatalysis technology has the potential to address both steadily rising global energy demand and environmental pollution issues [1]. Water-splitting photoelectrochemical cells (PECs) have several advantages over other renewable energy device technologies since a PEC harvests plentiful and inexhaustible solar energy and converts water into hydrogen, which is a portable, high energy

density fuel. The performance of a photoelectrocatalyst depends on several aspects of a complex process, such as band positions, light harvesting, charge excitation, charge separation, charge transfer and surface electrocatalytic reactions [2]. Therefore the overall efficiency is a function of the efficiencies of all these individual steps, a fact that has motivated a search for ideal photocatalytic systems with optimized electronic bandgaps, facile charge separation, adequate carrier transport, morphologies and dimensions comparable to carrier diffusion lengths, high density of active surface sites, etc. Several oxide/sulfide based semiconductors such as TiO_2, ZnS, CdS, ZnO, $BiVO_4$, and complex composition materials *i.e.* La- and Rh-codoped $SrTiO_3$ ($SrTiO_3$:La, Rh) have been explored as photoanodes for water splitting. However, no photoelectrocatalyst has achieved a satisfactory performance for the deployment of PEC technology at an industrial scale [3, 4].

Graphitic carbon nitride (g-C_3N_4), a metal-free two-dimensional conjugated semiconducting polymer, composed of tris-*s*-triazine (C_6N_7) units linked together with tertiary nitrogen is currently being intensely studied for the realization of efficient artificial photosynthetic systems [2, 5-14]. g-C_3N_4 and related graphenic frameworks are particularly promising for PECs because of the following reasons: (i) They are constituted of earth abundant elements (carbon and nitrogen) (ii) They have relatively simple, scalable and inexpensive methods of synthesis (iii) g-C_3N_4 has a moderate bandgap (2.7 eV) with suitable band-edge positions (Ecb: -1.1 V and Evb: +1.6 V *vs* NHE at pH-0) for water-splitting and (iv) They possesses good thermal stability (stable up to 600 °C), photochemical stability (non-photocorrosive) and chemical stability (resistant to strong acids and bases) [2, 6, 7, 9, 15]. Despite these attractive features, g-C_3N_4 suffers from fast charge carrier recombination and narrow visible light absorption limited to the blue region of the solar spectrum [14]. Many attempts have been made to improve the light absorption capability, such as surface

area modification, doping with P, N, F, I, Cl, B *etc* and incorporation of N-rich units in cross-linked heptazine framework [16-21]. The synthesis of F-doped carbon nitride using ammonium fluoride (NH_4F) as a dopant material revealed that F atoms are bonded to C atoms in the corners and bays through transformation of sp^2 C to sp^3 C [22]. This shifts the highest occupied molecular orbital (HOMO) and lowest unoccupied molecular orbital (LUMO) positions and results in a reduced bandgap and enhanced photocatalytic performance [22]. Bulk g-C_3N_4 possesses hydrogen bonding between graphitic sheets, which remains a potential source of localized interlayer charge recombination, detrimental to photocatalytic activity. Therefore, few-layered or single-layered crystalline sheets (with periodic heptazine units) are highly desirable to realize better charge separation through the suppression of inter-layer charge recombination [23-25]. Several attempts have been made to transform bulk g-C_3N_4 into few-layered or single-layered nanosheets namely, solvent exfoliation, oxidation, varying precursors, *etc* [26-29]. In this regard, using sheets-forming-precursor is most attractive as it precludes hazardous chemicals involved in chemical exfoliation [30, 31]. Lu et al. demonstrated the use of ammonium chloride (NH_4Cl) with dicyandiamide; the carbon nitride precursor released NH_3 and HCl gases during thermal annealing which blew dicyandiamide derived polymers into numerous large bubbles, which behaved as gas templates and yielded few layered g-C_3N_4 nanosheets [30]. In another report Liu et al. showed that NH_4Cl not only assisted in the transformation into sheets but excess NH_4Cl also facilitated chlorine intercalation in between g-C_3N_4 sheets which acted as a charge transport gallery to reduce the recombination rate and improved the porous structure [19]. Motivated by these findings, we have demonstrated the synthesis of few-layered fluorine-doped and chlorine-intercalated carbon nitride nanosheets (CNF-Cl) using dicyandiamide as a precursor for carbon nitride skeleton while NH_4F and NH_4Cl were used as sources for F and Cl (sheets determining agent) respectively.

Recently, earth abundant ternary compound semiconductors from the bismuth oxyhalide (BiOX, X = Cl, Br, I) family have received significant attention for their high photocatalytic activities owing to small bandgaps (1.7 – 1.9 eV) and suitable nanomorphology. Narrow bandgap BiOI possesses a layered crystal structure in which positive $[Bi_2O_2]^{2+}$ layers are interleaved with negatively charged iodide slabs [32-36]. This creates an internal built-in electric field which facilitates the separation and transport of photogenerated electron-hole pairs [37-41]. Another attractive feature of the BiOI band structure lies in its dispersive nature, which enables excitation of electrons through multiple pathways [40]. Despite the above mentioned attributes, BiOI remains a poor photocatalyst due to many unwanted features such as low conductivity, fast charge recombination, *etc* [38, 40]. The key scientific challenge therefore is to achieve a much higher photocatalytic and/or photoelectrochemical performance using BIOI-based platforms. Recently, certain research groups have reported the photocatalytic performances of BiOI-based type-II heterostructures [42-49]. In this work, we have attempted to suppress interlayer charge recombination of bulk carbon nitride by two efficient, facile and cost-effective steps, namely (1) formation of few layered fluorine-doped and chlorine-intercalated nanosheets (CNF-Cl) and (2) *in situ* growth of heterojunctions of CNF-Cl with BiOI. The resulting BiOI/CNF-Cl heterojunctions showed remarkable improvement in the measured photocurrent densities under AM1.5 G one sun illumination. BiOI/CNF-Cl demonstrated excellent photoelectrochemical H_2 evolution rate (19.71 μmol h^{-1}) and Faradaic efficiency (82.83%) in comparison to pristine BiOI and CNFCl. The superior performance of the nanocomposite catalysts is attributed to the enhanced charge separation and improved light harvesting capability.

2.0 Results and discussion

2.1 Synthesis, Morphological, structural and compositional analysis

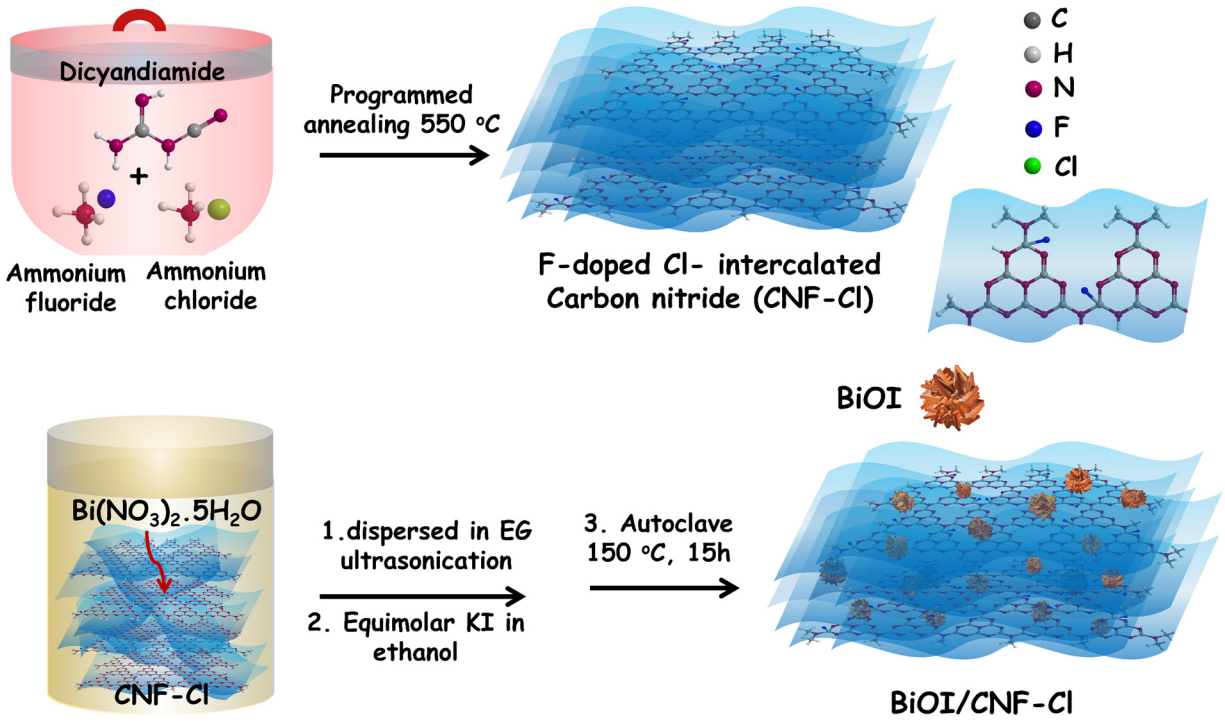

Figure 1. Synthetic outline for the preparation of F doped Cl-intercalated g-C_3N_4 (CNF-Cl) and BiOI/CNF-Cl nanostructured heterojunction.

The synthesis of few layered F doped Cl-intercalated carbon nitride (CNF-Cl) sheets was pursued by thermal annealing of dicyandiamide, NH_4F and NH_4Cl at 550 ºC through a slight modification of previous reported methods (Figure 1) [19, 22, 30]. In this synthesis protocol dicyandiamide serves as the source of carbon and nitrogen. High temperature condensation polymerization of dicyandiamide yields heptazine (C_6N_7) units containing g-C_3N_4 framework *via* melamine, melon, melem, intermediates and evolution of ammonia. NH_4F facilitates fluorine doping of heptazine moieties because of degradation of NH_4F during thermal annealing and released F atom make bonds to heptazine ring carbons. The incorporation of electron withdrawing F atoms in g-C_3N_4 scaffold transforms some sp^2 hybridized C atoms in to sp^3 C which partially distorted in-plane symmetry of conjugated network resulting in the shifting of HOMO and LUMO positions (band

edge positions) and a reduction of the bandgap [22]. NH_4Cl plays a dual role in the synthesis - 1) facilitating the formation of few layered sheets due to release of NH_3 and HCl gases at elevated temperature that blow dicyandiamide-derived polymers into numerous large bubbles, yielding F doped g-C_3N_4 nanosheets [30] and 2) chlorine intercalation in between g-C_3N_4 layers. The chlorine intercalation in between few layered F-doped carbon nitride sheets provides interlayer galleries for better charge migration along with uplifting of the conduction band and a narrower bandgap [19]. The detailed experimental protocols and physicochemical characterization methodologies *i.e.* Fourier transform infrared spectroscopy (FTIR), Electrochemical impedance spectroscopy (EIS) and Mott-Schottky plots, efficiency calculations (ABPE, IPCE, APCE and Faradaic efficiency) and reuse experiment results are provided in Supporting Information.

The fine morphological attributes of BiOI/CNFCl composite to discern the presence of CNF-Cl sheets and dendritic BiOI nanoplates were determined using high-resolution transmission electron microscopy (HR-TEM). The HR-TEM image of BiOI/CNF-Cl clearly shows dense and more crystalline domains correspond to BiOI while less dense domains indicate CNF-Cl in the heterostructure (Figure 2a-2c). High magnification HRTEM image displayed lattice fringes of CNF-Cl and BiOI with interplanar *d*-spacing of 0.32 and 0.28 nm assigned to (002) plane of CNF-Cl and (110) plane of BiOI respectively (Figure 2b-2c) [45, 50]. The obtained *d*-spacings were in excellent agreement with XRD results (Figure 3a). The presence of (002) plane specific to graphitic structure suggests CNF-Cl sheets were stacked together in the BiOI/CNF-Cl nanocomposites. The overlapping of these materials onto each other is unambiguously evident in Figure 2b, where both the crystal lattices are identified in the same region. Figure 2e shows the FESEM image of BiOI/CNF-Cl composite, where both stacked layers comprising the two materials are visible, in agreement with the TEM images. A closer observation reveals the

hydrothermally synthesized dendritic BiOI nanoplates scaffolded with CNF-Cl framework. Elemental mapping BiOI/CNF-Cl heterojunction in scanning transmission electron microscopy (STEM) mode clearly showed even distribution of the Bi, I and O in dense region and C, N and F in both less dense and dense regions (Figures 2f-2l respectively). Due to the partial overlap of Bi and Cl peaks, pristine CNF-Cl was also mapped which clearly demonstrates the presence of Cl in nanosheets [51]. Figures 2m-3q show the constituent elements of CNF-Cl, C, N, F and Cl respectively.

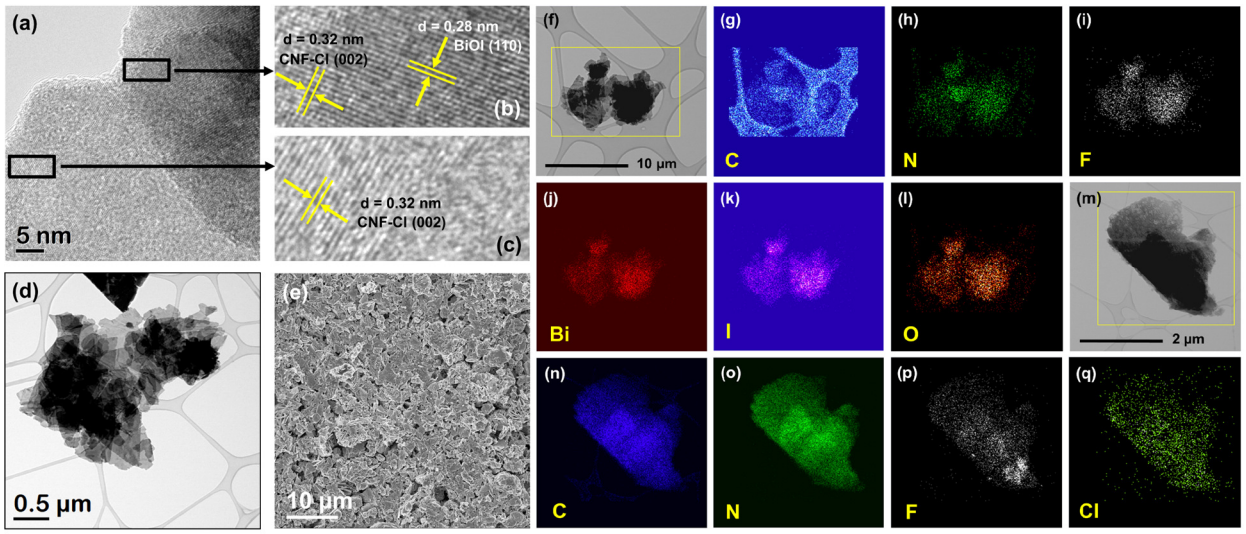

Figure 2. (a) HRTEM image of 50% BiOI/CNF-Cl; (b) and (c) Selected magnified regions of (a) showing crystal planes of CNF-Cl and BiOI; (d) Bright field STEM image of 50% BiOI/CNF-Cl; (e) FESEM image of 50% BiOI/CNF-Cl film, (f) and (m) Bright field STEM images of 50% BiOI/CNF-Cl and pristine CNF-Cl respectively; (g-l) EDX elemental mapping of 50% BiOI/CNF-Cl under STEM mode for C (g), N (h), F (i), Bi (j), I (k) and O (l); (n-q) EDX elemental mapping of pristine CNF-Cl under STEM mode for C (n), N (o), F (p), and Cl (q).

The XRD spectra of CNF-Cl exhibited a broad peak centered at ~ 27.1° corresponding to the (002) plane which indicates interlayer stacking of conjugated aromatic sheets, with a 0.33 nm interlayer *d* spacing, while the other small peak at 13.1° corresponding to the (100) reflection

represents in-plane repetition of tri-*s*-triazine unit, consistent with previously reported data for g-C_3N_4 (Figure 3a) [13, 52]. This *d* spacing was slightly higher than reported for pristine g-C_3N_4 (0.32 nm), which might be due to the increased repulsion between sheets caused by out-of-plane F atoms [53]. The XRD plot for pristine BiOI demonstrated all the peaks associated with tetragonal phase of BiOI which was in good agreement with reported literature [43, 54]. As expected, the XRD peak intensities of BiOI decrease, while these intensities increase for CNF-Cl with the increase of CNF-Cl wt% in the BiOI/CNF-Cl composites. The appearance of both (002) and (100) peaks of CNF-Cl in the composite heterostructures, confirms the presence of CNF-Cl with preserved graphitic carbon nitride framework.

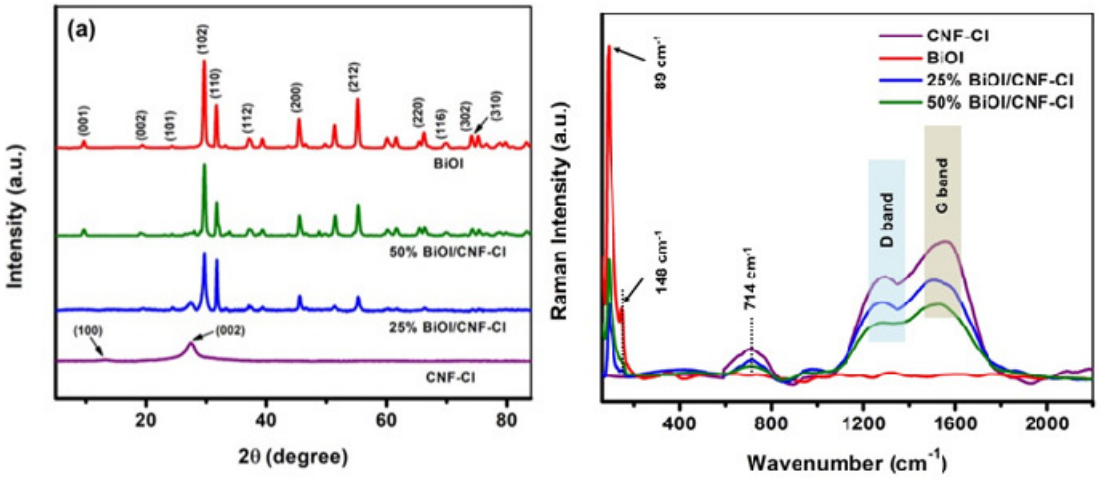

Figure 3. (a) X-Ray diffractograms of pristine BiOI, BiOI/CNF-Cl composites and pristine CNF-Cl and (b) Raman spectra (λ_{exc} = 785 nm) of pristine CNF-Cl, pristine BiOI and BiOI/CNF-Cl heterostructures.

Figure 3b shows the Raman spectra for pristine CNF-Cl, BiOI and BiOI/CNF-Cl the heterostructures. Two characteristic peaks in between 1300 and 1600 cm^{-1} assigned to D and G bands of graphene-based materials were clearly visible in the Raman spectra of the pristine CNF-Cl and their composites with BiOI. The D band is associated with the out of plane vibrations of sp^3 carbon atoms, representative of defects and disorder in the systems, and the G band is assigned

to E_{2g} phonons at Γ point, which originates from the in-plane vibrations of sp^2 carbon atoms [55, 56]. Unlike graphene or graphene oxide based materials, carbon nitride based materials do not exhibit sharp D and G bands due to plenty of defects and short range ordered structure. The relative intensities of the Raman peaks corresponding to the D and G bands, provide an indication of defects and order in carbon nitride materials. In pristine bulk g-C_3N_4, $I_D/I_G = 0.36$, which increases to 0.82 in fluorinated g-C_3N_4 due to increased disorder [57]. In both pristine CNF-Cl and the CNF-Cl containing composites prepared by us, the ratio $I_D/I_G \sim 0.74$, close to that of fluorinated g-C_3N_4. The almost unchanged intensity ratio (I_D/I_G) of these bands, in the BiOI/CNF-Cl nanocomposites, compared to the pristine CNF-Cl is indicative of unperturbed crystallinity, order and in-plane sp^2 domain size in the nanocomposites, consistent with the XRD results. The relatively smaller peak around 714 cm^{-1}, which has been attributed to the out of plane C–C vibrations [58], is present in the spectrum of both pristine CNF-Cl and BiOI/CNF-Cl heterostructures. The sharp Raman peaks at the lower wavenumbers are vibrational modes of BiOI. The peak at 148 cm^{-1} is assigned to the E_g internal Bi–I stretching mode [59]. As expected, the relative intensities of the D and G bands of CNF-Cl decreased in BiOI/CNF-Cl composite as the wt% of BiOI increased.

2.2 Photophysical properties

Prior to the photocatalytic testing experiments, we studied the photophysical properties of conventional bulk g-C_3N_4, as-prepared CNF-Cl, pristine BiOI, and BiOI/CNF-Cl nanocomposites using UV-Vis spectroscopy (collected in diffuse reflectance mode), steady state photoluminescence (SSPL) spectroscopy and time resolved photoluminescence (TRPL). Figure 4a shows the UV-Vis absorption spectra of these materials. CNF-Cl shows an absorption band ~ 270 nm due to π→π* transition that originates from the two-coordinated nitrogen vacancy in the conjugated ring, while another band around 380 nm with band tail extended up to 500 nm, is

believed to originate from the n→π* transition, associated with N lone pair electrons in triazine/heptazine rings [60, 61]. The fluorine doping and chlorine intercalation in CNF-Cl improves visible harvesting over conventional g-C_3N_4 by generating a *ca*. 50 nm redshift in the optical absorption. Despite the red-shifted absorption, the bandgap of pristine CNF-Cl is still relatively large, while the composite heterojunction with a small bandgap material, such as BiOI improves the light harvesting capability to a significant extent. Pristine BiOI exhibits a band-edge at ~ 680 nm. Two clear band edges, corresponding to CNF-Cl and BiOI, can be seen from the plots of nanocomposite heterostructures (Figure 4a). Further, bandgaps of the as-prepared materials were estimated using Tauc plots (Figure 4b) through extrapolation of the linear regions of graphs between $(\alpha h\nu)^{1/2}$ *vs* hν on abscissa where α is the absorption coefficient, *h* is Planck's constant and ν is the frequency of light. The effective bandgaps of g-C_3N_4, pristine CNF-Cl, pristine BiOI, 10% BiOI/CNF-Cl, 25% BiOI/CNF-Cl, 50% BiOI/CNF-Cl and 75% BiOI/CNF-Cl were found to be 2.46, 2.05 eV, 1.88 eV, 1.86 eV, 1.88 eV, 1.81 eV and 1.88 eV respectively. The observed bandgap of g-C_3N_4 was slightly lower than reported value for bulk g-C_3N_4 (2.7 eV) which might be due to the use of dicyandiamide precursor instead of melamine and programmed annealing which also affects the degree of polymerization and stacking pattern modifying the bandgap [62-65]. The reduction in the bandgap of fluorinated carbon nitride, compared to g-C_3N_4 was attributed to the successful doping of F into the C–N matrix, in contrast to counterion-bounded F [22]. The pristine BiOI and BiOI/CNF-Cl composites demonstrate almost similar bandgap (~1.88 eV) suggesting major absorption was dominated by BiOI. These bandgap values clearly indicate the superior light absorption capabilities of the nanocomposite heterostructures, compared to pristine CNF-Cl.

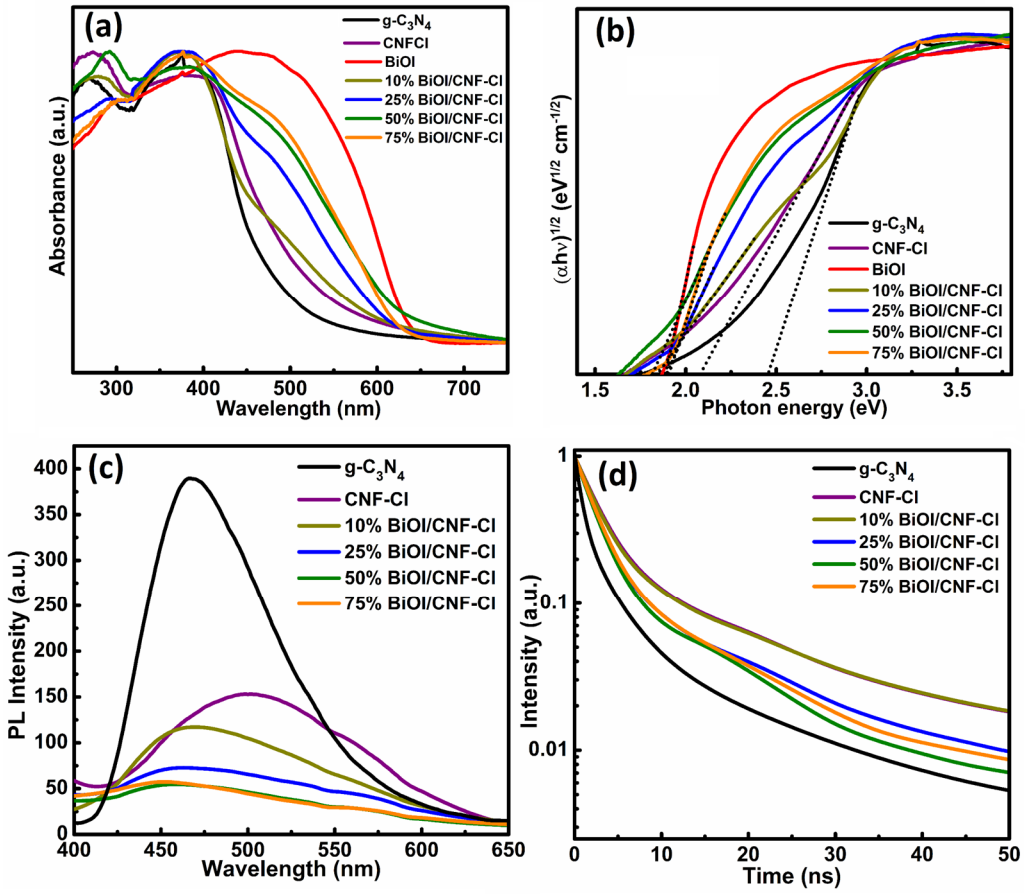

Figure 4. (a) UV-Vis absorption spectra collected in diffuse reflectance spectroscopy (DRS) mode and (b) Tauc plots for the determination of the effective optical bandgaps of pristine g-C_3N_4, pristine CNF-Cl, pristine BiOI and BiOI/CNF-Cl heterostructures. (c) Steady state photoluminescence spectra (λ_{exc} = 360 nm) and (d) Time resolved photoluminescence spectra (λ_{exc} = 405 nm) for conventional g-C_3N_4, pristine CNF-Cl and BiOI/ CNF-Cl heterostructures.

Steady state photoluminescence (SSPL) spectra of the investigated pristine and composite materials are presented in Figure 4c. CNF-Cl shows an intense and broad SSPL peak centered at ~ 500 nm, indicative of a fast band-to-band radiative recombination process of photogenerated electrons and holes. The emission peak of CNF-Cl was red-shifted by *ca.* 50 nm from the emission peak of bulk g-C_3N_4, and is similar to the absorption shift seen in Figure 4c. The ~ 50 nm redshifts in both the absorption and emission spectra clearly demonstrate the distinct optoelectronic

properties of CNF-Cl in comparison to g-C_3N_4. The SSPL signals for BiOI/CNF-Cl heterostructures were quenched significantly compared to the pristine CNF-Cl, suggesting efficient charge transfer between BiOI and CNF-Cl. These results were similar to the previously reported works of nanocomposite systems comprising BiOI and g-C_3N_4 [44, 45]. Notice that a significant blue shift can be observed in the emission spectra of the nanocomposites, relative to pristine CNF-Cl. While no conclusive reason has been identified, electronic interactions between CNF-Cl and BiOI might be responsible for this shift through affecting the relative strength of the $\pi \rightarrow \pi^*$ and $n \rightarrow \pi^*$ transitions in the composite heterostructures. Time resolved photoluminescence (TRPL) spectra were collected (Figure 4d), and fitted to a tri-exponential decay function of the form:

$$I(t) = A_1 e^{-t/\tau 1} + A_2 e^{-t/\tau 2} + A_3 e^{-t/\tau 3} \quad (1)$$

where, A_1, A_2 and A_3 represent normalized percentage of each decay components and τ_1, τ_2 and τ_3 are the lifetimes of each decay component respectively. The presence of three lifetime decay components in most of the fitted curves, is in accord with previously reported TRPL data for carbon nitride-based materials [66, 67]. Table 1 shows the lifetime decay constants, average lifetime and curve-fitting parameters for conventional g-C_3N_4, pristine CNF-Cl and BiOI/CNF-Cl nanocomposites. The longest lifetime component in the emission decay g-C_3N_4 (14.83 ns in Table 1) was extended to 61.73 ns in CNF-Cl together with a strong enhancement of its relative intensity, which provides definitive evidence for the suppression of non-radiative recombination pathways due to chlorine intercalation-mediated increased separation between adjacent stacked sheets. The PL decay data taken together with the UV-Vis and steady state PL spectra provides further evidence for the distinct optoelectronic properties of CNF-Cl in comparison to bulk g-C_3N_4.

The carbon nitride framework is constituted of tri-*s*-triazine (heptazine; C_6N_7) units where sp^2 hybridized carbon and nitrogen overlap together to give σ and π bonding and σ* and π* antibonding molecular orbitals. Nonbonded lone pair (LP) electrons on the secondary nitrogens (C-N=C) also contribute to the delocalized π system which promotes formation of an intermediate energy LP-π hybridized π molecular orbital (LP-π hybridized MO) [67-71]. The observed first lifetime decay component for g-C_3N_4 and CNF-Cl was attributed to direct band-to-band radiative recombination (antibonding σ*→ LP-π hybridized MO transition and antibonding π*→ LP-π hybridized MO) while the second decay component arises due to nonradiative relaxation of σ* electron to π* orbital followed by radiative recombination with LP-π hybridized MO (σ*→π* (non-radiative) and π*→ LP-π hybridized MO (radiative) [72-74]. The value of the first lifetime and its relative contribution for g-C_3N_4 was found to be 0.715 ns and 0.765 respectively while for CNF-Cl, this value was determined to be 2.117 ns and 0.78 ns respectively. The increased first lifetime of CNF-Cl was attributed to the addition of F atom in heptazine motif breaking the symmetry and transforming some sp^2 hybridized carbons to sp^3 carbon which increases the population of relatively long lived σ*→ LP-π hybridized MO transitions [22]. The second decay lifetime of CNF-Cl increased to 12.96 ns in comparison to g-C_3N_4 (3.097 ns) which suggests that the introduction of more electronegative F bonded to sp^3 C in heptazine motif promotes long lived σ*→LP-π hybridized MO transition via σ*→π* non-radiative relaxation mechanism. Further, decrease in relative contribution (0.194) of the second lifetime of CNF-Cl compared to g-C_3N_4 (0.321) supports the theory that creation of sp^3 defects via fluorine atom doping reduces the contribution of direct π*→ LP-π MO recombination due to the reduced conjugation [75, 76]. Interestingly, the third lifetime specific to inter/intra-sheet radiative recombination for CNF-Cl was found to be 61.726 ns which was much higher than bulk g-C_3N_4 (14.827 ns). The increased

third lifetime suggest better inter-sheets charge migration due to Cl-intercalation which provide interlayer galleries [19]. Further formation of few layered sheets also facilitate charge separation and reduce recombination resulting in an increased lifetime [66, 67, 77, 78].

Table 1. Summary of fitted parameters obtained from time resolved photoluminescence plots shown in Figure 6b for conventional g-C_3N_4, pristine CNF-Cl and BiOI/CNF-Cl composites.

Photocatalyst	τ_1 (ns)/A_1	τ_2 (ns)/A_2	τ_3 (ns)/A_3	Average lifetime τ (ns)	Reduced χ^2	Adj. R^2
g-C_3N_4	0.715/0.765	3.097/0.321	14.827/0.059	8.84	1.91×10^{-5}	0.999
CNF-Cl	2.117/0.780	12.960/0.194	61.726/0.023	23.06	2.90×10^{-7}	0.999
10% BiOI/CNF-Cl	0.072/0.467	3.880/0.398	20.832/0.129	14.53	2.67×10^{-6}	0.999
25% BiOI/CNF-Cl	0.153/0.441	2.867/0.441	16.626/0.114	10.89	7.75×10^{-7}	0.999
50% BiOI/CNF-Cl		1.829/0.776	12.960/0.137	8.02	1.46×10^{-6}	0.999
75% BiOI/CNF-Cl		1.934/0.801	12.900/0.150	8.02	5.40×10^{-7}	0.999

The average lifetime (τ_{avg}) is a good metric to quantitatively evaluate the effectiveness of electron-hole separation in the photocatalysts and was determined using the following equation:

$$\tau_{avg} = (A_1\tau_1^2 + A_2\tau_2^2 + A_3\tau_3^2)/ (A_1\tau_1 + A_2\tau_2 + A_3\tau_3) \quad (2)$$

The average lifetimes of CNF-Cl, 10% BiOI/CNF-Cl, 25% BiOI/CNF-Cl, 50% BiOI/CNF-Cl, 75% BiOI/CNF-Cl were found to be 23.06, 14.53, 10.89, 8.02 and 8.02 ns respectively. The lifetimes of both the longest and second-longest PL decay components of CNF-Cl monotonically decreased in the blends with BiOI with the effect saturating at a blend concentration of 50% and higher. Average lifetimes are significantly reduced for the nanocomposites compared to the pristine CNF-Cl, consistent with the quenching of SSPL intensity discussed earlier in this section.

Moreover, the SSPL quenching follows same trend with the TRPL lifetime decay, with the maximum quenching and decay occur for the 50% BiOI/CNF-Cl and 75% BiOI/CNF-Cl heterojunctions. The obtained steady state and transient photoluminescence spectroscopy results suggest better charge separation in the nanocomposites compared to the constituent pristine materials.

2.3 Photoelectrochemical activity test for water splitting

PEC tests were carried out using three electrode system (photocatalyst deposited FTO as anode, Pt cathode and Ag/AgCl reference electrode and Na_2SO_4). From Figure 5a, it can be seen that the obtained photocurrent density for pristine CNF-Cl was a mere 0.28 mA cm^{-2} at 1.23V *vs* RHE (water oxidation potential) which suggests fast intersheet recombination of photogenerated electron hole pairs. Further, due to a bandgap of 2.05 eV, the CNF-Cl absorbs only the high energy fraction of the visible spectrum to generate electron hole pairs. Similarly, the obtained value of photocurrent density for pristine BiOI was found to be a mere 0.40 mA cm^{-2}. However, after formation of heterojunction with CNF-Cl, the photoresponse of the resulting BiOI/CNF-Cl hybrid increased dramatically (Figure 8a). Among various wt% of BiOI (10% BiOI/CNF-Cl, 25% BiOI/CNF-Cl, 50% BiOI/CNF-Cl and 75% BiOI/CNF-Cl) the nanocomposite composed of 50% BiOI and 50% CNF-Cl displayed the highest photocurrent density (1.28 mA cm^{-2}). The photocurrent densities for 10% BiOI/CNF-Cl, 25% BiOI/CNF-Cl and 75% BiOI/CNF-Cl heterostructures were measured to be 0.34, 0.95 and 1.01 mA cm^{-2} respectively. The improved PEC performance of BiOI/CNF-Cl hybrid structure clearly demonstrates improved charge separation due to formation of heterojunction and better charge transport on the surface of conjugated carbon nitride sheets. To validate the true origin of photocurrent and instantaneous

photoresponse of materials, photocurrent was measured during light On-Off cycles which clearly displayed rise and drop in photocurrent in On-Off cycles (Figure 5b).

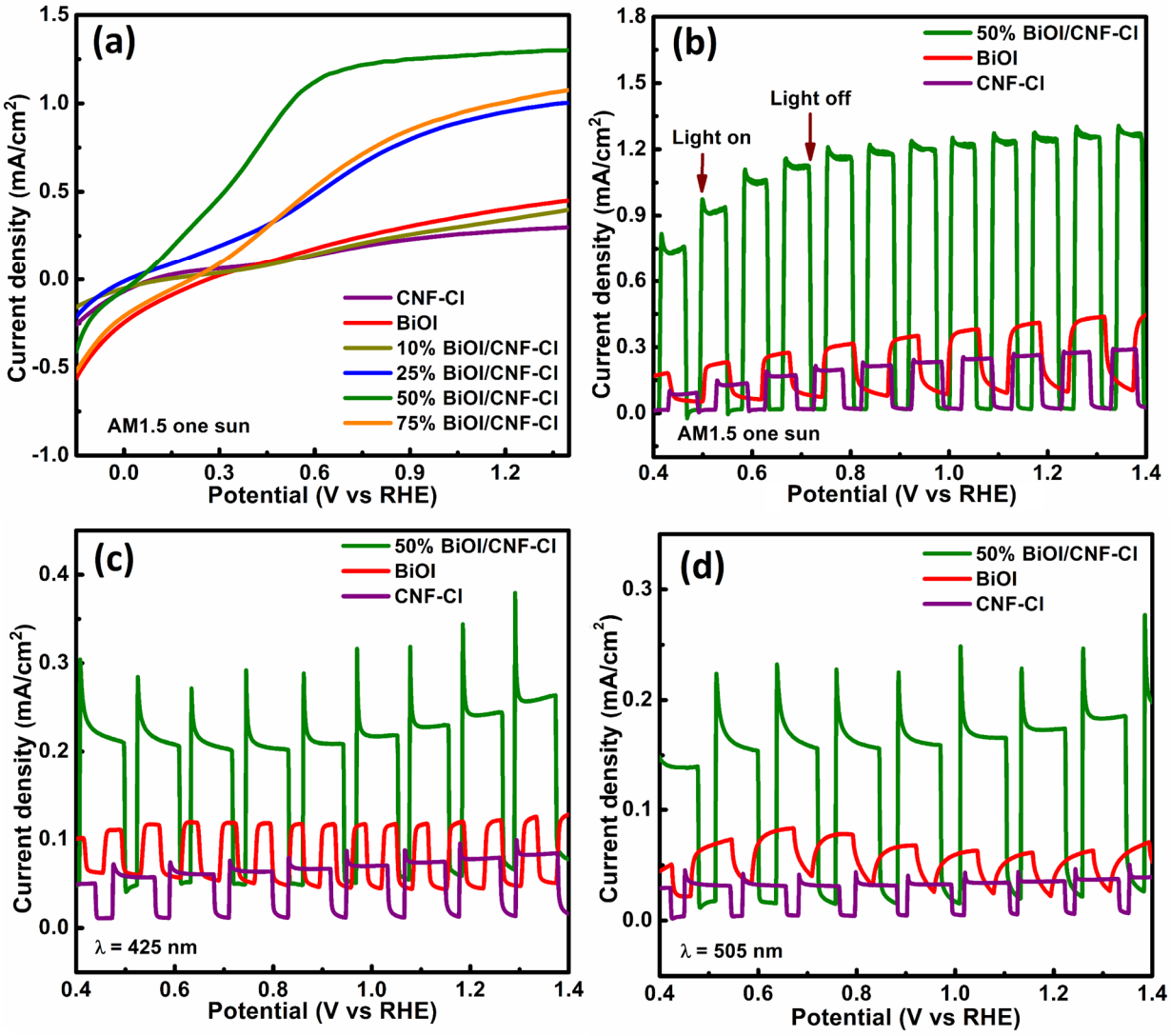

Figure 5. (a) Photocurrent of pristine CNF-Cl, pristine BiOI and BiOI/CNF-Cl composite catalysts under AM1.5 G one sun illumination; (b), (c) and (d) Light on-off experiment for pristine CNF-Cl, pristine BiOI and 50% BiOI/CNF-Cl under AM1.5 G one sun illumination, 425 nm (54.15 mW cm^{-2}) and 505 nm (40.48 mW cm^{-2}) LEDs respectively.

To discern the PEC performance of the synthesized materials at visible wavelengths, the photocurrent response of materials during On-Off cycles was measured using monochromatic 425 nm and 505 nm wavelength LEDs having a power density of 54.15 and 40.48 mW cm^{-2} respectively at the surface of photoanode (Figures 5c and 5d). In comparison to pristine CNF-Cl and BiOI, the photocurrent response of heterostructured BiOI/CNF-Cl was much higher which demonstrates synergistic charge separation due to the formation of a heterojunction. The photocurrent densities for pristine CNF-Cl, BiOI and heterostructure BiOI/CNF-Cl under 425 nm monochromatic irradiation were obtained to be 0.08, 0.12 and 0.24 mA cm^{-2} respectively (Figure 8c). Under 505 nm irradiation the photocurrent densities for CNF-Cl, BiOI and heterostructure BiOI/CNF-Cl were found to be 0.04, 0.06 and 0.18 mA cm^{-2} respectively (Figure 5d). 505 nm photons are primarily absorbed by BiOI (see UV-Vis spectra in Figure 4a). Under illumination by the 505 nm LED, the pristine BiOI photoanode exhibits a slow rise in photocurrent during each On cycle (red curve in Figure 5d) which is characteristic of the presence of a large number of carrier traps; the photocurrent rises as traps are filled by photogenerated carriers. On the other hand, the BiOI/CNF-Cl photoanode displayed intense spikes instantaneously during light on cycles which decreased and reached a steady state. The spike in photocurrent is due to the instantaneous movement of a large number of photogenerated charge carriers because of fast charge separation in the BiOI/CNF-Cl heterojunction. We attribute the near-exponential decrease in current to reach steady state during each on cycle to trap mediated recombination in BiOI. The EIS Nyquist plot revealed a smaller semicircle arc for the 50% BiOI/CNF-Cl in comparison to pristine films and other blends evidencing a lower charge transfer resistance at semiconductor-electrolyte interface for this composition. Further, the calculated recombination lifetime values were shorter for BiOI/CNFCl heterojunctions suggesting lower resistance for hole transfer to electrolyte and better

charge separation within the heterostructures (see Section 4.0 in ESI, Figure S2-S4 and Table S1). The positive slope in Mott-Schottky plot (C^{-2}–V curves) shows *n*-type conduction of the materials and the calculated flat band positions (V_{FB}) of CNF-Cl, BiOI, 25% BiOI/CNF-Cl, and 50% BiOI/CNF-Cl were calculated to be -0.461, -0.418, -0.521 and -0.675 *vs* NHE scale at pH-0 (ESI; Section 4.0, Figure S2 and S4).

The light harvesting performance and efficiency of subsequent transformation into electrical energy were calculated from the diagnostic efficiencies under applied bias and irradiation conditions (Figure 6) [79, 80]. The applied bias photon-to-current efficiencies (ABPEs) of pristine CNF-Cl and BiOI were found to be 0.08 and 0.11 % respectively (Figure S5 in ESI†) while ABPE% of 10% BiOI/CNF-Cl, 25% BiOI/CNF-Cl, 50% BiOI/CNF-Cl and 75% BiOI/CNF-Cl heterostructures were calculated to be 0.09, 0.31, 0.71, and 0.34 % respectively. The maximum ABPE% was found for 50% BiOI/CNF-Cl which was 8.75 times higher than pristine CNF-Cl and 6.45 times higher than pristine BiOI respectively. The incident photon-to-current efficiency (IPCE) or external quantum efficiencies (EQEs) of CNF-Cl, BiOI and 50% BiOI/CNF-Cl were calculated to be 0.43, 0.64 and 1.29% at 425 nm and 0.24, 0.36 and 1.09 % for 505 nm irradiation (Figure 5a). Furthermore, absorbed photon-to-current efficiency (APCE) or internal quantum efficiency (IQE) for CNF-Cl, BiOI and BiOI/CNF-Cl under 425 nm irradiation was calculated to be 0.53, 0.73 and 1.61 while under 505 nm these values was found 0.49, 0.42 and 1.54 % respectively (Figure 6a). The similarity of the EQE and APCE values merely confirms almost complete light harvesting at 425 nm and 505 nm wavelengths due to the strong visible absorption of the BiOI/CNF-Cl composites. The EQE values measured under 425 nm and 505 nm LED illumination are low despite excellent photon harvesting (Figure 4a), superior charge separation (Figures 4c, 4d and Figures S2-S4) and enhanced recombination suppression (Section 2.5) in the BiOI/CNF-Cl

heterojunctions. We attribute the low PEC quantum yields to the large exciting binding energy (E_b) of 0.20 -0.35 eV (~ 10 times thermal energy at room temperature) in heptazine motif carbon nitrides [81, 82]. As previously mentioned, fluorination of carbon nitride introduces structural distortions that reduce the conjugation length and further increase E_b [83]. The large values of E_b mean that only a small fraction of the photogenerated excitons are dissociated into free carriers.

2.4 Photoelectrochemical H_2 evolution measurement

A three-electrode H-cell containing the deposited materials as the photoanode, Pt cathode and Ag/AgCl reference electrode was used for the measurement of evolved H_2 (Figure S6). The evolved hydrogen at the Pt counter electrode was analyzed using a gas chromatograph (GC) equipped with a pulse discharge ionization detector (PDD) (Figure S7). The observed H_2 evolution rates using CNF-Cl, BiOI and BiOI/CNF-Cl as a photoelectrocatalyst were found to be 0.71, 4.35 and 19.71 μmol h^{-1}, respectively. The theoretical H_2 evolution rates, based on photocurrent densities for CNF-Cl, BiOI and BiOI/CNF-Cl were calculated to be 5.22, 7.46 and 23.80 μmol h^{-1} respectively. From these values, the Faradaic efficiencies for CNF-Cl, BiOI and BiOI/CNF-Cl were calculated to be 13.51, 58.29 and 82.83 (percent), respectively (Figure 6b). Water splitting occurs at higher applied bias which also promotes side reaction. In such conditions, due to lower reduction potential of SO_4^{2-} ions (+0.172 V vs NHE at pH-0) of Na_2SO_4, it competes with proton reduction resulting in poor Faradaic efficiency. PEC performance and subsequent characterization of reused BiOI/CNF-Cl showed almost identical photoactivity and structural features as freshly prepared materials, indicating demonstrate resilience and durability of the materials (ESI; Section 5.0 Figure S8-S10).

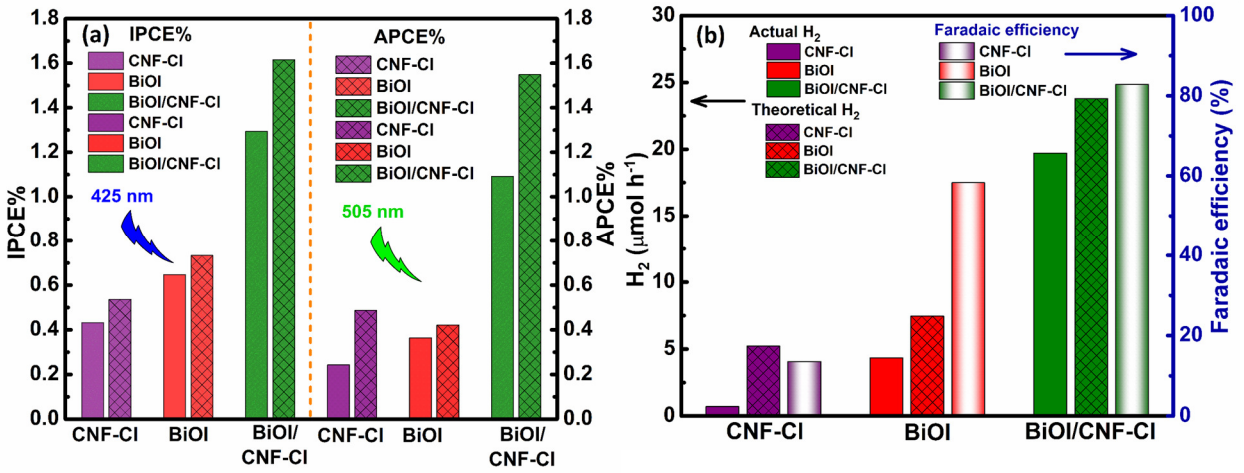

Figure 6. (a) IPCE% and APCE% of CNF-Cl, BiOI and BiOI/CNF-Cl heterojunction. (b) Graph of actually observed H_2 evolution rate determined using GC, theoretically calculated evolution rates from photocurrent and corresponding Faradaic efficiencies.

Table 2. Photoelectrochemical H_2 evolution rate determined experimentally using GC, theoretically calculated evolution rates from photocurrent, and corresponding Faradaic efficiencies.

Sample	Experimentally evolved H_2 ($\mu mol\ h^{-1}\ cm^{-2}$)	Theoretically calculated H_2 ($\mu mol\ h^{-1}\ cm^{-2}$)	Faradaic Efficiency (%)
CNF-Cl	0.71	5.22	13.51
BiOI	4.35	7.46	58.29
BiOI/CNF-Cl	19.71	23.80	82.83

2.5 Photo-Kelvin probe force microscopy

Kelvin-probe force microscopy (KPFM) has been used for simultaneous structural and electronic property mapping of photovoltaic and photocatalytic materials [84, 85]. Herein, we performed KPFM to image carrier photogeneration (Figure 7). Surface potential, which is the difference between contact potentials of the tip and semiconductor surface, was determined both in the dark and under illumination (425 nm LED). The difference between these two surface potentials can be termed as the surface photopotential. Upon illumination, the quasi-Fermi level of a *n*-type

semiconductor rises (w.r.t E_{vac}) and thus the difference between the tip work function and semiconductor surface work function increases, compared to the difference in dark condition.

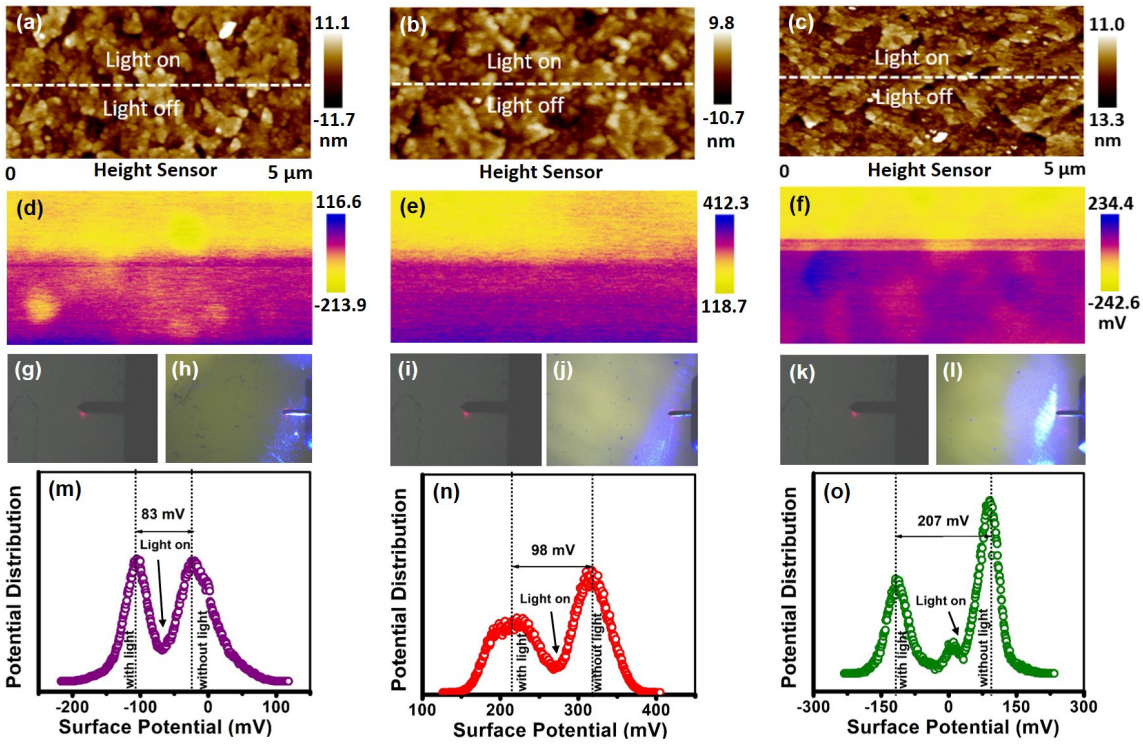

Figure 7. (a)-(c) Surface topographic AFM images of pristine CNF-Cl, pristine BiOI and 50% BiOI/CNF-Cl respectively; (d)-(f) KPFM surface potential mappings under light (LED 425 nm) (yellow region) and in the dark (purple region) of the samples corresponding to (a)-(c); (g), (i) and (k) AFM tip scan in dark and (h), (j) and (l) AFM tip scan under light (425 nm LED) for the samples corresponding to (a)-(c); (m)-(o) Surface potential distribution in the dark and under illumination condition (LED 425 nm) for pristine CNF-Cl, pristine BiOI and 50% BiOI/CNF-Cl respectively.

By observing the surface photopotential of different semiconductors, we can quantitatively analyze the photogenerated charge carriers and study the comparative photoresponse. KPFM data was acquired for pristine CNF-Cl, pristine BiOI and 50% BiOI/CNF-Cl. Surface topographic images, surface potential maps and surface potential distributions for all the photocatalysts are

shown in Figure 7. Dark and illumination conditions are clearly visible in the surface potential mapping and distribution plots. The comparative analysis shows that the nanocomposite photocatalyst 50% BiOI/CNF-Cl has the largest surface photopotential of 207 mV, while pristine CNF-Cl and BiOI have surface photopotential values of 83 mV and 98 mV respectively. These KPFM data indicates the highest charge carrier (electron) separation occurs in BiOI/CNF-Cl heterostructure compared to the pristine materials. The order of the negative shift of surface potentials for these three materials nicely correlates with their obtained photocurrents (Figure 8). Therefore, the KPFM data corroborates the view of enhanced charge separation in the heterostructured photocatalyst, discussed earlier.

2.6 Photoresponse enhancement mechanism

To explain the improved photocatalytic performance a plausible mechanism was proposed based on electronic band structure and existing literature (Figure 8) [46, 86-88]. The process of overall water splitting includes two half reactions 1) hydrogen evolution reaction (HER) at the cathode by reduction of protons to hydrogen and 2) oxygen evolution reaction (OER) by oxidation of water to oxygen at anode. To achieve efficient water splitting, the conduction band (E_{CB}) position of the semiconductor should be more negative than 0.00 eV *vs* NHE (reduction potential of proton, H^+/H_2) and valence band (E_{VB}) should be more positive than +1.23 eV *vs* NHE (oxidation potential of water (H_2O/O_2). These requirements suggest that the bandgap of materials should be higher than 1.23 eV [14, 83, 89]. However, wide bandgap compromises visible light absorption and results in a poor light harvesting efficiency. The optical bandgap of CNF-Cl was found to be 2.05 eV and the E_{CB} and E_{VB} positions were calculated to be -0.461 and +1.589 V *vs* NHE. For BiOI, the bandgap value was 1.82 eV and respective conduction (E_{CB}) and valence (E_{VB}) band positions was found to be -0.418 and +1.402 V *vs* NHE. The bandgaps and band edge positions of CNF-Cl and

BiOI demonstrate that both materials individually fulfill the requirement of water splitting. However, observed photocurrents for pristine CNF-Cl and BiOI were extremely low which can be explained by fast band-to-band charge recombination in BiOI and interlayer charge recombination in CNF-Cl. After the formation of heterojunction between BiOI and CNF-Cl, the PEC performance of BiOI/CNF-Cl was dramatically enhanced. The improved PEC performance of BiOI/CNF-Cl nanostructures can be explained on the basis of Fermi level alignment which leads to formation of a Type II (staggered) *n*-*n* heterojunction between BiOI and CNF-Cl [90-92]. CNF-Cl displayed strong *n*-type characteristics in Mott Schottky measurement which implies its Fermi level lies just below the conduction band. BiOI displayed weak *n*-type character implying an intermediate position of Fermi level between E_{CB} and E_{VB}. Heterostructure formation of BiOI with CNF-Cl aligns the Fermi levels in the two materials, and is accompanied by a built-in field at the interface between the two semiconductors [93]. During Fermi level alignment, the conduction band of BiOI bends downward while conduction band of CNF-Cl experiences upward band bending as depicted in Figure 8 [94].

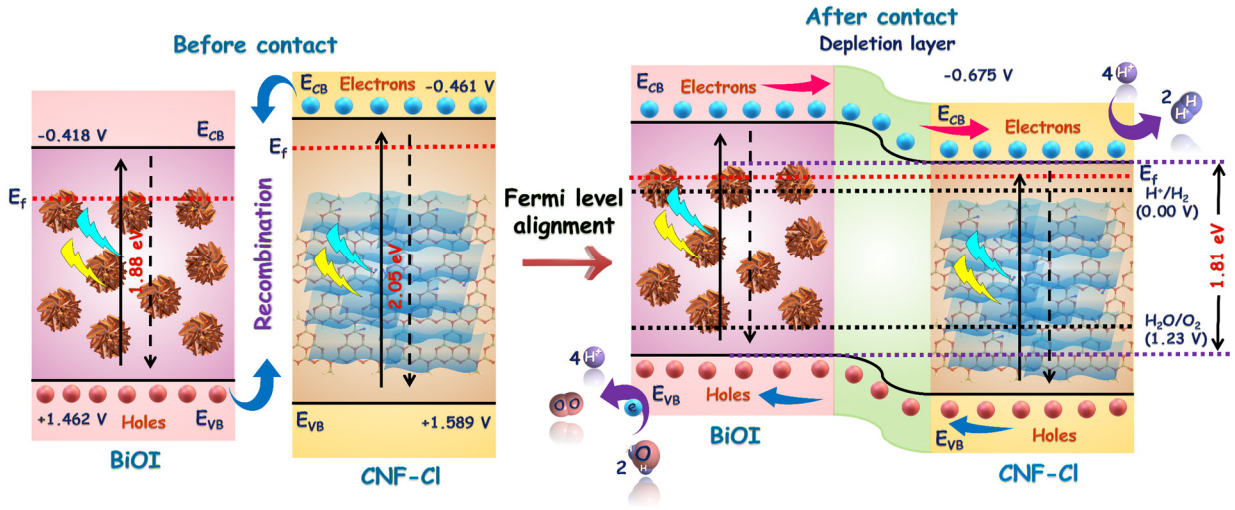

Figure 8. Proposed mechanism of charge separation in BiOI/CNF-Cl composite photoanodes.

3.0 Conclusion

We have demonstrated the synthesis of few layered fluorine-doped and chlorine-intercalated carbon nitride nanosheets (CNF-Cl) with a reduced bandgap. CNF-Cl also exhibits a red-shifted emission spectrum and substantially longer PL lifetime components in comparison to g-C_3N_4. The likely origin of these lifetime components in the emission decays of g-C_3N_4 and CNF-Cl were explained. These newly synthesized F-doped and Cl-intercalated carbon nitride nanosheets were used to develop heterostructured photocatalysts with earth abundant BiOI. BiOI was found to exhibit weak *n*-type conduction while CNF-Cl was found to be a strongly *n*-type semiconductor. A broad swathe of characterization data including steady state and time-resolved PL spectra, Mott-Schottky plots. KPFM data and photoelectrochemical *J-V* curves are consistent with enhanced charge separation in BiOI/CNF-Cl hybrids due to the formation of a type-II *n-n* heterojunction. The enhanced charge separation and extended light harvesting (band-edge of 680 nm) results in significantly increased photoelectrochemical performance compared to the stand-alone constituent materials with photocurrent densities as high as 1.28 mA cm^{-2} observed under AM1.5 G one sun illumination. The energy conversion efficiency metric known as ABPE% for the top performing heterojunction (50% BiOI/CNF-Cl) was 8.75 times higher than pristine CNF-Cl and 6.45 times higher than pristine BiOI. Reusability tests and characterization of used photoanodes demonstrated the required robustness and are indicative of long-term operational stability. Furthermore, unusual electronic interactions between BiOI and CNF-Cl were observed that manifested as a significant blue-shift in the steady-state emission spectra of the BiOI/CNF-Cl heterostructures but with little or no effect in the absorption spectra.

Acknowledgements

The authors thank NSERC, NRC, CMC Microsystems, Future Energy Systems and CFI for direct and indirect (equipment use) financial support. U.K.T. acknowledges scholarship support from Alberta Innovates. The conduct of this work used several routine characterization tools at the University of Alberta Nanofab (a fee-based facility). Prof. Thomas Thundat is kindly acknowledged for allowing the use of the KPFM facility in his lab and Prof. Alkiviathes Meldrum is thanked for allowing the use of the time-resolved PL facility in his lab.

References

[1] Tachibana Y, Vayssieres L and Durrant J R 2012 Artificial photosynthesis for solar water-splitting *Nature Photonics* **6** 511

[2] Zheng Y, Lin L, Wang B and Wang X 2015 Graphitic carbon nitride polymers toward sustainable photoredox catalysis *Angewandte Chemie International Edition* **54** 12868-84

[3] Wen J, Xie J, Chen X and Li X 2017 A review on g-C 3 N 4 -based photocatalysts *Appl. Surf. Sci.* **391** 72-123

[4] Wang Q, Hisatomi T, Jia Q, Tokudome H, Zhong M, Wang C, Pan Z, Takata T, Nakabayashi M and Shibata N 2016 Scalable water splitting on particulate photocatalyst sheets with a solar-to-hydrogen energy conversion efficiency exceeding 1% *Nature materials* **15** 611

[5] Wen J, Xie J, Chen X and Li X 2017 A review on g-C3N4-based photocatalysts *Applied surface science* **391** 72-123

[6] Naseri A, Samadi M, Pourjavadi A, Moshfegh A Z and Ramakrishna S 2017 Graphitic carbon nitride (gC 3 N 4)-based photocatalysts for solar hydrogen generation: recent advances and future development directions *Journal of Materials Chemistry A* **5** 23406-33

[7] Wang X, Maeda K, Thomas A, Takanabe K, Xin G, Carlsson J M, Domen K and Antonietti M 2009 A metal-free polymeric photocatalyst for hydrogen production from water under visible light *Nature materials* **8** 76

[8] Lin Q, Li L, Liang S, Liu M, Bi J and Wu L 2015 Efficient synthesis of monolayer carbon nitride 2D nanosheet with tunable concentration and enhanced visible-light photocatalytic activities *Applied Catalysis B: Environmental* **163** 135-42

[9] Yin S, Han J, Zhou T and Xu R 2015 Recent progress in gC 3 N 4 based low cost photocatalytic system: activity enhancement and emerging applications *Catalysis Science & Technology* **5** 5048-61

[10] Rajender G, Choudhury B and Giri P 2017 In situ decoration of plasmonic Au nanoparticles on graphene quantum dots-graphitic carbon nitride hybrid and evaluation of its visible light photocatalytic performance *Nanotechnology* **28** 395703

[11] Choudhury B 2019 *Nanophotocatalysis and Environmental Applications*: Springer) pp 167-209
[12] Ong W-J, Tan L-L, Ng Y H, Yong S-T and Chai S-P 2016 Graphitic carbon nitride (g-C3N4)-based photocatalysts for artificial photosynthesis and environmental remediation: are we a step closer to achieving sustainability? *Chemical reviews* **116** 7159-329
[13] Thomas A, Fischer A, Goettmann F, Antonietti M, Müller J-O, Schlögl R and Carlsson J M 2008 Graphitic carbon nitride materials: variation of structure and morphology and their use as metal-free catalysts *Journal of Materials Chemistry* **18** 4893-908
[14] Kumar P, Boukherroub R and Shankar K 2018 Sunlight-driven water-splitting using two-dimensional carbon based semiconductors *Journal of Materials Chemistry A* **6** 12876-931
[15] Kumar P, Vahidzadeh E, Thakur U K, Kar P, Alam K M, Goswami A, Mahdi N, Cui K, Bernard G M and Michaelis V K 2019 C3N5: A Low Bandgap Semiconductor Containing an Azo-Linked Carbon Nitride Framework for Photocatalytic, Photovoltaic and Adsorbent Applications *Journal of the American Chemical Society* **141** 5415-36
[16] Jiang L, Yuan X, Pan Y, Liang J, Zeng G, Wu Z and Wang H 2017 Doping of graphitic carbon nitride for photocatalysis: a reveiw *Appl. Catal. B-Environ.* **217** 388-406
[17] Zhang G, Zhang M, Ye X, Qiu X, Lin S and Wang X 2014 Iodine modified carbon nitride semiconductors as visible light photocatalysts for hydrogen evolution *Advanced Materials* **26** 805-9
[18] Wang Y, Li H, Yao J, Wang X and Antonietti M 2011 Synthesis of boron doped polymeric carbon nitride solids and their use as metal-free catalysts for aliphatic C–H bond oxidation *Chemical Science* **2** 446-50
[19] Liu C, Zhang Y, Dong F, Reshak A, Ye L, Pinna N, Zeng C, Zhang T and Huang H 2017 Chlorine intercalation in graphitic carbon nitride for efficient photocatalysis *Appl. Catal. B-Environ.* **203** 465-74
[20] Mane G P, Talapaneni S N, Lakhi K S, Ilbeygi H, Ravon U, Al-Bahily K, Mori T, Park D H and Vinu A 2017 Highly Ordered Nitrogen-Rich Mesoporous Carbon Nitrides and Their Superior Performance for Sensing and Photocatalytic Hydrogen Generation *Angewandte Chemie International Edition* **56** 8481-5
[21] Ran J, Ma T Y, Gao G, Du X-W and Qiao S Z 2015 Porous P-doped graphitic carbon nitride nanosheets for synergistically enhanced visible-light photocatalytic H 2 production *Energy & Environmental Science* **8** 3708-17
[22] Wang Y, Di Y, Antonietti M, Li H, Chen X and Wang X 2010 Excellent visible-light photocatalysis of fluorinated polymeric carbon nitride solids *Chemistry of Materials* **22** 5119-21
[23] Yang S, Gong Y, Zhang J, Zhan L, Ma L, Fang Z, Vajtai R, Wang X and Ajayan P M 2013 Exfoliated graphitic carbon nitride nanosheets as efficient catalysts for hydrogen evolution under visible light *Advanced Materials* **25** 2452-6
[24] Schwinghammer K, Mesch M B, Duppel V, Ziegler C, Senker J r and Lotsch B V 2014 Crystalline carbon nitride nanosheets for improved visible-light hydrogen evolution *Journal of the American Chemical Society* **136** 1730-3

[25] Ou H, Lin L, Zheng Y, Yang P, Fang Y and Wang X 2017 Tri-s-triazine-Based Crystalline Carbon Nitride Nanosheets for an Improved Hydrogen Evolution *Advanced Materials* **29** 1700008
[26] Zhang J, Chen Y and Wang X 2015 Two-dimensional covalent carbon nitride nanosheets: synthesis, functionalization, and applications *Energy & Environmental Science* **8** 3092-108
[27] Zhang X, Xie X, Wang H, Zhang J, Pan B and Xie Y 2012 Enhanced photoresponsive ultrathin graphitic-phase C3N4 nanosheets for bioimaging *Journal of the American Chemical Society* **135** 18-21
[28] Xu J, Zhang L, Shi R and Zhu Y 2013 Chemical exfoliation of graphitic carbon nitride for efficient heterogeneous photocatalysis *Journal of Materials Chemistry A* **1** 14766-72
[29] She X, Xu H, Xu Y, Yan J, Xia J, Xu L, Song Y, Jiang Y, Zhang Q and Li H 2014 Exfoliated graphene-like carbon nitride in organic solvents: enhanced photocatalytic activity and highly selective and sensitive sensor for the detection of trace amounts of Cu 2+ *Journal of Materials Chemistry A* **2** 2563-70
[30] Lu X, Xu K, Chen P, Jia K, Liu S and Wu C 2014 Facile one step method realizing scalable production of gC 3 N 4 nanosheets and study of their photocatalytic H 2 evolution activity *Journal of Materials Chemistry A* **2** 18924-8
[31] Wu M, Yan J M, Tang X n, Zhao M and Jiang Q 2014 Synthesis of Potassium-Modified Graphitic Carbon Nitride with High Photocatalytic Activity for Hydrogen Evolution *ChemSusChem* **7** 2654-8
[32] Bhachu D S, Moniz S J, Sathasivam S, Scanlon D O, Walsh A, Bawaked S M, Mokhtar M, Obaid A Y, Parkin I P and Tang J 2016 Bismuth oxyhalides: synthesis, structure and photoelectrochemical activity *Chemical Science* **7** 4832-41
[33] Cheng H, Huang B and Dai Y 2014 Engineering BiOX (X= Cl, Br, I) nanostructures for highly efficient photocatalytic applications *Nanoscale* **6** 2009-26
[34] Guan M, Xiao C, Zhang J, Fan S, An R, Cheng Q, Xie J, Zhou M, Ye B and Xie Y 2013 Vacancy associates promoting solar-driven photocatalytic activity of ultrathin bismuth oxychloride nanosheets *Journal of the American Chemical Society* **135** 10411-7
[35] Zhang X, Ai Z, Jia F and Zhang L 2008 Generalized one-pot synthesis, characterization, and photocatalytic activity of hierarchical BiOX (X= Cl, Br, I) nanoplate microspheres *The Journal of Physical Chemistry C* **112** 747-53
[36] Meng X and Zhang Z 2018 New insight into BiOX (X= Cl, Br, and I) hierarchical microspheres in photocatalysis *Materials Letters* **225** 152-6
[37] Liu Q-C, Ma D-K, Hu Y-Y, Zeng Y-W and Huang S-M 2013 Various bismuth oxyiodide hierarchical architectures: alcohothermal-controlled synthesis, photocatalytic activities, and adsorption capabilities for phosphate in water *ACS applied materials & interfaces* **5** 11927-34
[38] Huang Y, Li H, Balogun M-S, Liu W, Tong Y, Lu X and Ji H 2014 Oxygen vacancy induced bismuth oxyiodide with remarkably increased visible-light absorption and superior photocatalytic performance *ACS applied materials & interfaces* **6** 22920-7
[39] Mera A C, Moreno Y, Pivan J-Y, Peña O and Mansilla H D 2014 Solvothermal synthesis of BiOI microspheres: Effect of the reaction time on the morphology and photocatalytic activity *Journal of Photochemistry and Photobiology A: Chemistry* **289** 7-13

[40] Gan J, Rajeeva B B, Wu Z, Penley D and Zheng Y 2016 Hydrogen-reduced bismuth oxyiodide nanoflake arrays with plasmonic enhancements for efficient photoelectrochemical water reduction *Electrochimica Acta* **219** 20-7
[41] Su J, Xiao Y and Ren M 2014 Direct hydrolysis synthesis of BiOI flowerlike hierarchical structures and it's photocatalytic activity under simulated sunlight irradiation *Catalysis Communications* **45** 30-3
[42] An H, Lin B, Xue C, Yan X, Dai Y, Wei J and Yang G 2018 Formation of BiOI/g-C3N4 nanosheet composites with high visible-light-driven photocatalytic activity *Chinese Journal of Catalysis* **39** 654-63
[43] Wang J-C, Yao H-C, Fan Z-Y, Zhang L, Wang J-S, Zang S-Q and Li Z-J 2016 Indirect Z-scheme BiOI/g-C3N4 photocatalysts with enhanced photoreduction CO2 activity under visible light irradiation *ACS applied materials & interfaces* **8** 3765-75
[44] Chou S-Y, Chen C-C, Dai Y-M, Lin J-H and Lee W W 2016 Novel synthesis of bismuth oxyiodide/graphitic carbon nitride nanocomposites with enhanced visible-light photocatalytic activity *RSC Advances* **6** 33478-91
[45] Di J, Xia J, Yin S, Xu H, Xu L, Xu Y, He M and Li H 2014 Preparation of sphere-like gC 3 N 4/BiOI photocatalysts via a reactable ionic liquid for visible-light-driven photocatalytic degradation of pollutants *Journal of Materials Chemistry A* **2** 5340-51
[46] Chang C, Zhu L, Wang S, Chu X and Yue L 2014 Novel mesoporous graphite carbon nitride/BiOI heterojunction for enhancing photocatalytic performance under visible-light irradiation *ACS applied materials & interfaces* **6** 5083-93
[47] Alam K M, Kumar P, Kar P, Thakur U K, Zeng S, Cui K and Shankar K 2019 Enhanced charge separation in g-C3N4–BiOI heterostructures for visible light driven photoelectrochemical water splitting *Nanoscale Advances* **1** 1460-71
[48] Liu B, Han X, Wang Y, Fan X, Wang Z, Zhang J and Shi H 2018 Synthesis of gC 3 N 4/BiOI/BiOBr heterostructures for efficient visible-light-induced photocatalytic and antibacterial activity *Journal of Materials Science: Materials in Electronics* **29** 14300-10
[49] Meng X, Jiang L, Wang W and Zhang Z 2015 Enhanced photocatalytic activity of BiOBr/ZnO heterojunction semiconductors prepared by facile hydrothermal method *International Journal of Photoenergy* **2015**
[50] Pan C, Xu J, Wang Y, Li D and Zhu Y 2012 Dramatic activity of C3N4/BiPO4 photocatalyst with core/shell structure formed by self-assembly *Advanced Functional Materials* **22** 1518-24
[51] Peng H, Chan C K, Meister S, Zhang X F and Cui Y 2008 Shape evolution of layer-structured bismuth oxychloride nanostructures via low-temperature chemical vapor transport *Chemistry of Materials* **21** 247-52
[52] Liu J, Zhang T, Wang Z, Dawson G and Chen W 2011 Simple pyrolysis of urea into graphitic carbon nitride with recyclable adsorption and photocatalytic activity *Journal of Materials Chemistry* **21** 14398-401
[53] Yuan S, Rösner M, Schulz A, Wehling T O and Katsnelson M I 2015 Electronic structures and optical properties of partially and fully fluorinated graphene *Phys. Rev. Lett.* **114** 047403

[54] Luo S, Xu J, Li Z, Liu C, Chen J, Min X, Fang M and Huang Z 2017 Bismuth oxyiodide coupled with bismuth nanodots for enhanced photocatalytic bisphenol A degradation: synergistic effects and mechanistic insight *Nanoscale* **9** 15484-93
[55] Ferrari A C and Robertson J 2000 Interpretation of Raman spectra of disordered and amorphous carbon *Physical review B* **61** 14095
[56] Dresselhaus M S, Jorio A, Hofmann M, Dresselhaus G and Saito R 2010 Perspectives on carbon nanotubes and graphene Raman spectroscopy *Nano letters* **10** 751-8
[57] Wang H, Zhang X, Xie J, Zhang J, Ma P, Pan B and Xie Y 2015 Structural distortion in graphitic-C3N4 realizing an efficient photoreactivity *Nanoscale* **7** 5152-6
[58] Chowdhury A, Cameron D and Hashmi M 1998 Vibrational properties of carbon nitride films by Raman spectroscopy *Thin Solid Films* **332** 62-8
[59] Bankar P K, Warule S S, Jadkar S R, Chaudhari N S and More M A 2016 Nanostructured BiOI–GO composite: facile room temperature synthesis with enhanced multifunctionality in field emission and photocatalytic activity *RSC Advances* **6** 83084-90
[60] Kumar A, Kumar P, Joshi C, Ponnada S, Pathak A K, Ali A, Sreedhar B and Jain S L 2016 A [Fe (bpy) 3] 2+ grafted graphitic carbon nitride hybrid for visible light assisted oxidative coupling of benzylamines under mild reaction conditions *Green Chemistry* **18** 2514-21
[61] Jorge A B, Martin D J, Dhanoa M T, Rahman A S, Makwana N, Tang J, Sella A, Corà F, Firth S and Darr J A 2013 H2 and O2 evolution from water half-splitting reactions by graphitic carbon nitride materials *The Journal of Physical Chemistry C* **117** 7178-85
[62] Hang L T, Lai N D, Phuong N T, Thang D V, Hung N M and Van Minh N 2018 Influence of annealing temperature on physical properties and photocatalytic ability of g-C3N4 nanosheets synthesized through urea polymerization in Ar atmosphere *Physica B: Condensed Matter* **532** 48-53
[63] Zhang W, Zhang Q, Dong F and Zhao Z 2013 The multiple effects of precursors on the properties of polymeric carbon nitride *International Journal of Photoenergy* **2013**
[64] Martin D J, Qiu K, Shevlin S A, Handoko A D, Chen X, Guo Z and Tang J 2014 Highly efficient photocatalytic H2 evolution from water using visible light and structure-controlled graphitic carbon nitride *Angewandte Chemie International Edition* **53** 9240-5
[65] Dong G and Zhang L 2012 Porous structure dependent photoreactivity of graphitic carbon nitride under visible light *Journal of Materials Chemistry* **22** 1160-6
[66] Yang P, Ou H, Fang Y and Wang X 2017 A facile steam reforming strategy to delaminate layered carbon nitride semiconductors for photoredox catalysis *Angewandte Chemie International Edition* **56** 3992-6
[67] Zhang Y, Pan Q, Chai G, Liang M, Dong G, Zhang Q and Qiu J 2013 Synthesis and luminescence mechanism of multicolor-emitting gC 3 N 4 nanopowders by low temperature thermal condensation of melamine *Scientific reports* **3** 1943
[68] Niu P, Liu G and Cheng H-M 2012 Nitrogen vacancy-promoted photocatalytic activity of graphitic carbon nitride *The Journal of Physical Chemistry C* **116** 11013-8
[69] Shalom M, Inal S, Fettkenhauer C, Neher D and Antonietti M 2013 Improving carbon nitride photocatalysis by supramolecular preorganization of monomers *Journal of the American Chemical Society* **135** 7118-21

[70] Kang Y, Yang Y, Yin L C, Kang X, Wang L, Liu G and Cheng H M 2016 Selective breaking of hydrogen bonds of layered carbon nitride for visible light photocatalysis *Advanced Materials* **28** 6471-7
[71] Shi R, Li Z, Yu H, Shang L, Zhou C, Waterhouse G I, Wu L Z and Zhang T 2017 Effect of Nitrogen Doping Level on the Performance of N-Doped Carbon Quantum Dot/TiO2 Composites for Photocatalytic Hydrogen Evolution *ChemSusChem* **10** 4650-6
[72] Chen L C, Teng C Y, Lin C Y, Chang H Y, Chen S J and Teng H 2016 Architecting nitrogen functionalities on graphene oxide photocatalysts for boosting hydrogen production in water decomposition process *Advanced Energy Materials* **6** 1600719
[73] Godin R, Wang Y, Zwijnenburg M A, Tang J and Durrant J R 2017 Time-resolved spectroscopic investigation of charge trapping in carbon nitrides photocatalysts for hydrogen generation *Journal of the American Chemical Society* **139** 5216-24
[74] Shalom M, Guttentag M, Fettkenhauer C, Inal S, Neher D, Llobet A and Antonietti M 2014 In situ formation of heterojunctions in modified graphitic carbon nitride: Synthesis and noble metal free photocatalysis *Chemistry of Materials* **26** 5812-8
[75] Liang Q, Li Z, Huang Z H, Kang F and Yang Q H 2015 Holey graphitic carbon nitride nanosheets with carbon vacancies for highly improved photocatalytic hydrogen production *Advanced Functional Materials* **25** 6885-92
[76] She X, Wu J, Zhong J, Xu H, Yang Y, Vajtai R, Lou J, Liu Y, Du D and Li H 2016 Oxygenated monolayer carbon nitride for excellent photocatalytic hydrogen evolution and external quantum efficiency *Nano Energy* **27** 138-46
[77] Niu P, Zhang L, Liu G and Cheng H M 2012 Graphene-like carbon nitride nanosheets for improved photocatalytic activities *Advanced Functional Materials* **22** 4763-70
[78] Meng N, Ren J, Liu Y, Huang Y, Petit T and Zhang B 2018 Engineering oxygen-containing and amino groups into two-dimensional atomically-thin porous polymeric carbon nitrogen for enhanced photocatalytic hydrogen production *Energy & Environmental Science* **11** 566-71
[79] Varghese O K and Grimes C A 2008 Appropriate strategies for determining the photoconversion efficiency of water photoelectrolysis cells: a review with examples using titania nanotube array photoanodes *Sol. Energy Mater. Sol. Cells* **92** 374-84
[80] Chen Z, Dinh H N and Miller E 2013 *Photoelectrochemical water splitting*: Springer)
[81] Melissen S, Le Bahers T, Steinmann S N and Sautet P 2015 Relationship between Carbon Nitride Structure and Exciton Binding Energies: A DFT Perspective *J. Phys. Chem. C* **119** 25188-96
[82] Sun J, Li X and Yang J 2018 The roles of buckled geometry and water environment in the excitonic properties of graphitic C3N4 *Nanoscale* **10** 3738-43
[83] Kumar P, Thakur U K, Alam K, Kar P, Kisslinger R, Zeng S, Patel S and Shankar K 2018 Arrays of TiO2 nanorods embedded with fluorine doped carbon nitride quantum dots (CNFQDs) for visible light driven water splitting *Carbon* **137** 174-87
[84] Spadafora E J, Demadrille R, Ratier B and Grévin B 2010 Imaging the carrier photogeneration in nanoscale phase segregated organic heterojunctions by Kelvin probe force microscopy *Nano letters* **10** 3337-42

[85] Wu M-C, Liao H-C, Cho Y-C, Tóth G, Chen Y-F, Su W-F and Kordas K 2013 Photo-Kelvin probe force microscopy for photocatalytic performance characterization of single filament of TiO 2 nanofiber photocatalysts *Journal of Materials Chemistry A* **1** 5715-20
[86] Roger I, Shipman M A and Symes M D 2017 Earth-abundant catalysts for electrochemical and photoelectrochemical water splitting *Nat. Rev. Chem.* **1** 0003
[87] Nellist M R, Laskowski F A, Lin F, Mills T J and Boettcher S W 2016 Semiconductor–electrocatalyst interfaces: theory, experiment, and applications in photoelectrochemical water splitting *Acc. Chem. Res.* **49** 733-40
[88] Indra A, Acharjya A, Menezes P W, Merschjann C, Hollmann D, Schwarze M, Aktas M, Friedrich A, Lochbrunner S and Thomas A 2017 Boosting Visible-Light-Driven Photocatalytic Hydrogen Evolution with an Integrated Nickel Phosphide–Carbon Nitride System *Angew. Chem., Int. Ed.* **56** 1653-7
[89] Hisatomi T, Kubota J and Domen K 2014 Recent advances in semiconductors for photocatalytic and photoelectrochemical water splitting *Chem. Soc. Rev.* **43** 7520-35
[90] Wang Y, Wang Q, Zhan X, Wang F, Safdar M and He J 2013 Visible light driven type II heterostructures and their enhanced photocatalysis properties: a review *Nanoscale* **5** 8326-39
[91] Li H, Zhou Y, Tu W, Ye J and Zou Z 2015 State-of-the-Art Progress in Diverse Heterostructured Photocatalysts toward Promoting Photocatalytic Performance *Adv. Funct. Mater.* **25** 998-1013
[92] Dashtian K, Ghaedi M, Shirinzadeh H, Hajati S and Shahbazi S 2018 Achieving enhanced blue-light-driven photocatalysis using nanosword-like VO2/CuWO4 type II n–n heterojunction *Chem. Eng. J. (Lausanne)* **339** 189-203
[93] Mu J, Miao H, Liu E, Feng J, Teng F, Zhang D, Kou Y, Jin Y, Fan J and Hu X 2018 Enhanced light trapping and high charge transmission capacities of novel structures for efficient photoelectrochemical water splitting *Nanoscale* **10** 11881-93
[94] Afroz K, Moniruddin M, Bakranov N, Kudaibergenov S and Nuraje N 2018 A heterojunction strategy to improve the visible light sensitive water splitting performance of photocatalytic materials *J. Mater. Chem. A* **6** 21696-718